RSC Advances

PAPER

Cite this: *RSC Adv.*, 2023, **13**, 12609

Folic acid–maltodextrin polymer coated magnetic graphene oxide as a NIR-responsive nano-drug delivery system for chemo-photothermal synergistic inhibition of tumor cells†

Tao Gong,‡[a] Xiaoyu Wang,‡[a] Huirui Zhu,[a] Chaochao Wen,[b] Qing Ma,[a] Xiaoning Li,[a] Meining Li,[a] Rui Guo*[a] and Wenting Liang *[b]

The combination of chemo-photothermal therapy with high efficiency and fewer side effects has a good application prospect in cancer treatment. It is of great significance to construct a nano-drug delivery system with cancer cell targeting, high drug loading and excellent photothermal conversion efficiency. Therefore, a novel nano-drug carrier MGO-MDP–FA was successfully constructed by coating folic acid-grafted maltodextrin polymers (MDP–FA) on the surface of Fe_3O_4-modified graphene oxide (MGO). The nano-drug carrier combined the cancer cell targeting of FA and the magnetic targeting of MGO. A large amount of anti-cancer drug doxorubicin (DOX) was loaded by π–π interaction, hydrogen bond interaction and hydrophobic interaction, with the maximum loading amount and loading capacity of 657.9 mg g^{-1} and 39.68 wt%, respectively. Based on the excellent photothermal conversion efficiency of MGO, MGO-MDP–FA showed good thermal ablation effect of tumor cells *in vitro* under NIR irradiation. In addition, MGO-MDP–FA@DOX showed excellent chemo-photothermal synergistic tumor inhibition *in vitro* (tumor cell killing rate reached 80%). In conclusion, the novel nano-drug delivery system MGO-MDP–FA constructed in this paper provides a promising nano-platform for chemo-photothermal synergistic treatment of cancer.

Received 7th April 2023
Accepted 15th April 2023

DOI: 10.1039/d3ra02306k

rsc.li/rsc-advances

1. Introduction

Photothermal therapy (PTT) has been widely used in cancer therapy with low toxic side effects, short acting time and remarkable curative effect. PTT utilizes photothermal conversion produced by photothermal agents with high photothermal conversion efficiency that convert light energy into heat to increase local temperature and induce cell death.[1–3] Therefore, the selection of a suitable photothermal agent is critical for photothermal therapy. At present, many photothermal agents have been discovered by researchers, including carbon nanomaterials,[4–8] gold nanomaterials,[9–11] silica dioxide,[12–14] *etc.* Among them, graphene oxide (GO) has been drawing attention as a novel carbon nanomaterial.

Graphene oxide is a two-dimensional carbon nanomaterial of sp^2-hybridized of carbon atoms with carboxyl, hydroxyl, and epoxide groups. It has been widely used in many fields due to its excellent physical and chemical properties.[15–17] In addition, carbon nanomaterials are often used as drug carriers for targeted delivery of chemotherapy drugs.[18–20] GO possesses large surface area and good water solubility, which can load a large number of hydrophobic chemotherapy drugs through π–π stacking and improve the water solubility of drugs.[21–23] However, GO tends to accumulate in physiological environments, which greatly limits its application as a drug carrier.[24,25]

In recent years, GO has been functionalized by hydrophilic polymers to improve its physiological stability for drug delivery.[26–28] Maltodextrin (MD) is a kind of hydrophilic polysaccharide hydrolyzed by amylase, with extremely rich hydroxyl groups, easy to modify and cross link to form polymers.[29,30] Maltodextrin has good water solubility and biocompatibility, and is often used as a stabilizer to improve the stability of substances. However, functionalized modifications occupy vast

[a]*Department of Biochemistry and Molecular Biology, Shanxi Medical University, Taiyuan 030001, China. E-mail: 15834151276@139.com*

[b]*Institute of Environmental Science, Department of Chemistry, Shanxi University, Taiyuan 030006, China. E-mail: liangwt@sxu.edu.cn*

† Electronic supplementary information (ESI) available: TEM images of MGO. Size distribution of MGO-MDP-FA measured by DLS. XRD of MGO. TGA curves of MGO in air. Temperature change curves of Fe_3O_4, GO and MGO solution with the concentration of 1.0 mg mL^{-1} under NIR laser irradiation (808 nm, 2.0 W cm^{-2}) for 0–5 min recorded by the thermal camera. Plot of calibration curves for DOX solution with different concentration. UV-Vis spectra of newly prepared MGO-MDP-FA@DOX aqueous solution placed for one month. The drug adsorption kinetic parameters for DOX on MGO-MDP–FA corresponded with Lagergren's pseudo-first-order model and Ho's pseudo-second-order model. Relevant parameters of Langmuir isotherm and Freundlich isotherm adsorption models for DOX by MGO-MDP–FA. See DOI: https://doi.org/10.1039/d3ra02306k

‡ These authors contributed equally.

functional groups on the GO surface, reducing the drug loading capacity of GO. Maltodextrin polymers have been reported to be capable of loading hydrophobic chemotherapeutic agents through molecular interactions (hydrophobic interactions, hydrogen bonding, *etc.*), enhancing the stability of GO while improving its drug loading performance.[31,32]

A targeting strategy can improve the selectivity of nanomaterials to tumor tissue and improve the effectiveness of chemotherapy drug delivery.[33,34] At present, active targeting has received extensive research and attention due to its high specificity and selectivity. Active targeting usually involves ligands with high affinity to specific surface molecules that are highly expressed on the surface of cancer cells. These ligands mainly include peptides, proteins, aptamers and so on.[35–37] Folic acid (FA) has the advantages of small size, poor immunogenicity, high utilization rate and simple conjugation, and is widely used in specific transport of chemotherapy drugs. Folate endows nanomaterials with active targeting by specifically binding to folate receptors (FR) that are highly expressed on the surface of tumor cells.[38,39]

In this study, magnetic graphene oxide (MGO) was prepared and its surface was modified with hydrophilic maltodextrin polymer (MDP) and active cancer targeting folic acid (FA) to construct a novel nano drug carrier MGO-MDP–FA. Finally, DOX and GO were anchored on the GO surface by π–π stacking and hydrophobic interaction to obtain multifunctional MGO-MDP–FA@DOX nanocomposites. The nano drug carrier has the advantages of high drug loading, biocompatibility, water solubility, tumor specific targeting and excellent drug loading capacity (DLC). Modified by maltodextrin polymer, the biocompatibility and physiological stability of nanoparticles were significantly improved. Modification of FA ligands allows nanoparticles to actively target tumor cells and the drug was further released under near-infrared light. Under the action of active targeting and NIR responsiveness, MGO-MDP–FA@DOX nanocomposites can effectively kill tumor cells in combination with chemotherapy and photothermal therapy, and achieve better therapeutic effect than single therapy (Scheme 1).

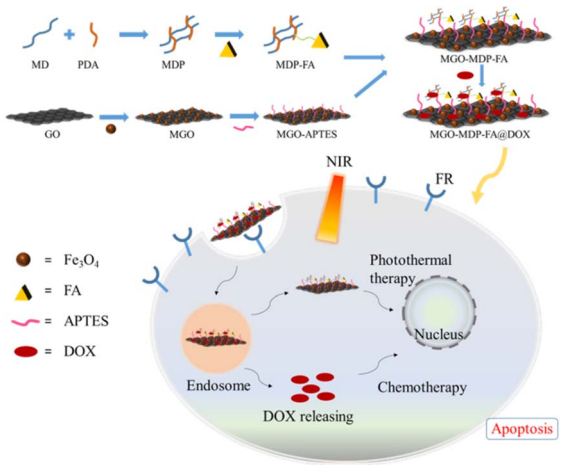

Scheme 1 The synthetic route and action diagram to cancer cell of MGO-MDP–FA nano-drug carrier.

2. Materials and methods

2.1 Materials

Graphene powder, folic acid (FA), 3-ammonia propyl-triethoxy silane (APTES), dicyclohexyl carbon imine (DCC), 4-dimethylaminopyridine (DMAP) and doxorubicin hydrochloride (DOX) were purchased from Aladdin Industrial Corporation.

Anhydrous ethanol, dimethyl sulfoxide (DMSO), ferric chloride and ferrous chloride were obtained from Tianjin Hengxing chemical reagent Co. Ltd. Maltodextrin (MD, 99%) was purchased from Shanghai Ciwei Chemical Technology Co., Ltd. Pyromellitic dianhydride (PDA) was purchased from Shanghai McLean Biochemical Technology Co., Ltd. Triethylamine is analytical pure, purchased from Tianjin Damao Chemical Reagent Company. Ammonia solution (NH_3, 25%) was supplied by Tianjin Beichen Reagent Factory. Phosphate Buffer Saline (PBS, pH 7.4) and 4′,6-diamidino-2-phenylindole (DAPI) were obtained from Boster Biological Technology Co., Ltd. Deionized water (DI water) was obtained from PURELAB Classic UVF system (ELGA, UK).

2.2 Synthesis of MDP–FA

MDP was firstly synthesized based on our previously published literature (the detailed synthesis process was described in ESI†).[40] In briefly, MD (3.0 g) was added to DMSO (12 mL) for stirring and dissolution. Then triethylamine (3.0 mL) was added and stirred for 10 min, and PMDA (4.0 g) was added and reacted at room temperature for 20 h. After the reaction, distilled water and acetone were respectively used to wash for 3 times and filtered, and then washed with distilled water for 3 times. The white powder MDP was obtained by freeze-drying.

Then the MDP–FA polymers were synthesized by esterification between MDP and FA. In briefly, FA (22 mg) was added into DMSO (20 mL) and stirred at 37 °C for 30 min. DCC (10.3 mg) and DMAP (6.1 mg) were added and stirred at room temperature for 1 h. Then MDP (22 mg) was added and stirred overnight at room temperature. After the reaction was completed, the suspension was centrifuged at 4000 rpm for 10 min and washed with anhydrous ethanol for 3 times. The white powder MDP–FA was obtained by centrifugation and vacuum drying.

2.3 Synthesis of MGO-MDP–FA

The MGO and aminated MGO (MGO-APTES) were synthesized according to our previously published literature (the detailed synthesis process was described in ESI†).[41,42] In briefly, MGO-APTES (50 mg) was dissolved in DMSO by ultrasonic, DCC (20 mg) and DMAP (12 mg) were added and stirred for 30 min at room temperature, and then the pre-synthesized MDP–FA was added and stirred for 24 h at room temperature. After the reaction was completed, the product was separated with a permanent magnet repeatedly and washed with anhydrous ethanol for 3 times. Finally, MGO-MDP–FA was obtained by vacuum drying and used in subsequent experiments. The yield of MGO-MDP–FA was determined by measuring the change of ultraviolet absorption of MDP–FA, and the yield of MGO-MDP–FA was 50%.

2.4 Characterization

Transmission electron microscopy (TEM) images were taken by a FEI Tecnai G2 F30 (Jeol, Japan) transmission electron microscope. Thermogravimetric Analysis (TGA) were recorded using a TA Instruments Q50 under flowing nitrogen atmosphere from room temperature to 800 °C. Magnetic properties were studied at room temperature by a Lakeshore 1600 vibrating sample magnetometer (VSM). X-ray diffraction (XRD) was carried out on a Bruker D8 Advance diffractometer in the 2θ range of 10–80°. Fourier transform infrared spectra (FTIR) were acquired by a Bruker FTIR spectrometer (INVENIO, GER). UV-VIS spectra were carried out on a UH5300 UV-VIS spectrophotometer (Tokyo, Japan). Fluorescence measurements were performed on a F-7000 fluorescence spectrophotometer (Tokyo, Japan). Fluorescence images were observed using a Nikon Eclipse Ti2 inverted fluorescent microscope (Tokyo, Japan). Laser irradiation was performed using an 808 nm laser (Hi-Tech Optoelectronics Co., Ltd).

2.5 Photothermal effect of MGO-MDP–FA

To measure the photothermal conversion performance, the PBS dispersions (1.0 mL) of MGO-MDP–FA with different concentrations (0.1, 0.4, 0.8, 1.0 mg mL^{-1}) and PBS (1.0 mL) were irradiated with NIR laser (808 nm, 2.0 W cm^{-2}) for 0–5 min. In addition, the PBS dispersions (1.0 mL) of MGO-MDP–FA with concentration of 1.0 mg mL^{-1} was irradiated by 808 nm NIR laser with different power densities (0.5, 1.0, 1.5, 2.0 W cm^{-2}) for 5 min. The temperature of all samples was monitored using a temperature measuring instrument (Testo AG 925).

In addition, in order to determine whether both Fe_3O_4 and GO are conducive to the photothermal effect of MGO-MDP–FA, we measured the photothermal properties of Fe_3O_4 and GO in concentration of 1.0 mg mL^{-1}, respectively under irradiation of NIR laser (808 nm, 2.0 W cm^{-2}) for 5 min.

2.6 Drug loading capability and mechanism of MGO-MDP–FA

To study drug releasing *in vitro*, MGO-MDP–FA (1.0 mg) was dispersed by ultrasound in 4.0 mL DOX solution (0.01 mg mL^{-1}) and vibrated avoid light at 200 rpm and 37 °C. At the certain time point, separating rapidly with a magnet and measuring the fluorescence intensity of supernatant. Then, the drug loading kinetics curve was drawn and Lagergren's pseudo first order kinetic model and Ho's pseudo second order kinetic model (the equations described in ESI†) were used to further analyze the load mechanism of drugs.

Subsequently, the drug loading capacity of MGO-MDP–FA was determined by isothermal adsorption experiment. In shortly, 1.0 mg MGO-MDP–FA was dispersed into a series of 4.0 mL DOX solutions with different concentrations and vibrated avoids light at 37 °C for 8 h. After separating with a permanent magnet, the supernatant was taken to measuring the fluorescence intensity at 558 nm, and the drug loading capacity (DLC) was calculated by the following eqn (1). In addition, we investigated the possible loading mechanism of DOX on MGO-MDP–FA by Langmuir model and Freundlich model (the equations described in ESI†).

$$\mathrm{DLC}(\%\mathrm{wt}) = \frac{W_{\mathrm{loaded}}}{W_{\mathrm{loaded}} + W_{\mathrm{material}}} \times 100\% \quad (1)$$

where, W_{loaded} represent the weight of the loaded drug, and W_{material} represent the weight of the nanomaterial.

2.7 Drug releasing experiments of MGO-MDP–FA

The drug releasing performance of DOX from MGO-MDP–FA was evaluated by fluorescence spectroscopy. Briefly, 1.0 mg MGO-MDP–FA@DOX was dispersed in 4.0 mL PBS at pH 5.3 and pH 7.4 respectively, and vibrated at 200 rpm in a 37 °C water bath. Then, separating with a permanent magnet rapidly at a specific time point, and taking the supernatant to measure the fluorescence intensity at 558 nm. Besides, in order to investigate the effect of NIR on drug releasing of DOX, the drug releasing performance of DOX from MGO-MDP–FA was researched with or without NIR (808 nm, 2.0 W cm^{-2}) light irradiation at different time points at pH 5.3 for 5 min and the amount of drug releasing was calculated by the following eqn (2):

$$\text{The percentage of drug released} = \frac{M_{\mathrm{raleased}}}{M_{\mathrm{loaded}}} \times 100\% \quad (2)$$

where, M_{released} and M_{loaded} represent the released amounts of drug and the loaded amounts of drug.

2.8 Biocompatibility and stability

The biocompatibility of MGO-MDP–FA was evaluated by hemolysis test *in vitro*. Briefly, 2.0 mL mouse blood was taken out and centrifuged at 4000 rpm for 30 min to obtain red blood cells, and then washed with PBS solution for three times and diluted with PBS. Then, 200 μL red blood cell was added to 1.0 mL deionized water or 1.0 mL PBS as the positive control and the negative control, respectively. Afterwards, adding 200 μL red blood cell to 1.0 mL MGO-MDP–FA solution with different concentrations (0.1–0.4 mg mL^{-1}) as experimental groups. Subsequently, incubating at 37 °C for 5 h and then centrifuged at 3000 rpm for 10 min. Finally, measuring the absorbance of the supernatant at 541 nm and calculated the hemolysis rate according to the following eqn (3):

$$\text{Hemolysis rate} = \frac{A_{\mathrm{s}} - A_{\mathrm{c}}}{A_{\mathrm{c}}(+) - A_{\mathrm{c}}(-)} \times 100\% \quad (3)$$

where, A_{s} represents the absorbance of the treatment groups with different concentrations and formulations, and $A_{\mathrm{c}}(+)$ and $A_{\mathrm{c}}(-)$ represent the absorbance of the distilled water group (positive control) and PBS group (negative control), respectively.

We also evaluated the stability of MGO-MDP–FA and MGO-MDP–FA@DOX by comparing the UV-vis spectra of MGO-MDP–FA and MGO-MDP–FA@DOX aqueous solution before and after one month of storage.

2.9 Cellular uptake of MGO-MDP–FA@DOX

Human hepatocellular carcinoma cells (HepG2), cervical carcinoma cells (HeLa), and normal cervical epithelial cells (HUCEC) were seeded into 12-well plates at a density of 5×10^4 cells per

well. After attaching to the wall, cells were incubated with MGO-MDP–FA@DOX (10 μg mL^{-1}) for 1 h, 3 h and 5 h, respectively. Furthermore, to evaluate the influence of FA on cell uptake properties, we firstly incubated cells with or without FA for 1 h, then incubated cells with MGO-MDP–FA@DOX at 37 °C for 5 h. Following by a washing step with PBS, cells were fixed by 4% paraformaldehyde at room temperature. After another washing step with PBS, the staining was performed with DAPI for 6 min. Finally, the cellular uptake of MGO-MDP–FA@DOX was observed under inverted fluorescence microscope. In addition, MGO-MDP without modification of FA was synthesized as a control to further evaluate the tumor targeting of FA by comparing the cellular uptake capacity of tumor cells for MGO-MDP and MGO-MDP–FA.

We further verified the *in vivo* tumor targeting ability of MGO-MDP–FA@DOX by intravenous injection. C57 mice (4 weeks, Shanxi Jietman Biotechnology Co., Ltd) were injected subcutaneously with U14 cells on the right hind limb and then randomly divided into 3 groups: (i) PBS; (ii) MGO-MDP; (iii) MGO-MDP–FA. When the tumor volume increased to about 100 mm^3, each group of mice were intravenously injected with the above corresponding formula. After injection for 24 h, each group was irradiated with NIR for 5 min. Then, infrared thermal camera was used for photothermal imaging of mouse tumor sites.

2.10 Evaluation of cytotoxicity *in vitro*

The vitro cytotoxicity of MGO-MDP–FA and the tumor cell killing efficiency of MGO-MDP–FA@DOX were carried out on HepG2, HeLa and HUCEC by Cell Counting Kit-8 (CCK-8). Firstly, cells were seeded into 96-well plates at a density of 1×10^4 cells per well. After incubating overnight, cells were treated with 100 μL fresh medium containing PBS, MGO-MDP–FA, DOX, MGO-MDP–FA@DOX, MGO-MDP–FA + NIR, MGO-MDP–FA@DOX + NIR each at different concentrations (10, 20, 40, 80 μg mL^{-1}) and incubated for 12 h in 37 °C, the groups requiring lighting treatment among them were stimulated with NIR (808 nm, 2.0 W cm^{-2}) for 10 min. After that, replacing the old culture medium with the fresh culture medium containing CCK-8 and incubating for 1 h. The absorbance of cells in each well at 450 nm was detected with an enzyme-linked immunoassay. Finally, the cells without any treatment were used as the control group, and the relative survival rate of cells in each group was calculated according to eqn (4):

$$\text{Cell viability} = \frac{\text{OD}_{\text{sample}}}{\text{OD}_{\text{control}}} \times 100\% \quad (4)$$

where, $\text{OD}_{\text{sample}}$ and $\text{OD}_{\text{control}}$ respectively represent the absorbance of cells in the treatment group and control group with different concentrations and formulations.

2.11 PTT/chemotherapy effect of MGO-MDP–FA@DOX

In order to further evaluate the PTT/Chemotherapy effect of MGO-MDP–FA@DOX *in vitro*, we analyzed the apoptosis and necrosis of cancer cells induced by MGO-MDP–FA@DOX using the Apoptosis and Necrosis Assay Kit (double staining method with Hoechst 33342 and PI). In brief, HepG2 and HeLa cells were inoculated in the 12-well plate at a density of 5×10^4 cells per well and divided into the following 6 groups: (i) PBS; (ii) MGO-MDP–FA; (iii) DOX; (iv) MGO-MDP–FA@DOX; (v) MGO-MDP–FA + NIR; (vi) MGO-MDP–FA@DOX + NIR. After adhering to the wall, cells were treated with culture medium containing above formula (10 μg mL^{-1}) for 24 h respectively, and the groups that needed lighting treatment were irradiated with NIR (808 nm, 2.0 W cm^{-2}) for 10 min. After that, staining cells with cell diluting fluid contains Hoechst 33342 (5.0 μL) and propidium iodide (PI, 5.0 μL) for 30 min under ice bath conditions. Finally, the inverted fluorescent microscope was observed the blue/red fluorescence of cancer cells under an inverted fluorescent microscope was used to observe the fluorescence of cells.

3. Results and discussion

3.1 Characterization of MGO-MDP–FA

TEM images showed that MGO presented as a sheet structure and decorated with abundant Fe_3O_4 MNPs, which were nearly spherical in shape and uniform in size uniformly distributed on the surface of MGO with an average particle size of 11 ± 2 nm (Fig. 1a and S1†). After removing the unbound MDP–FA, the MGO-MDP–FA was obtained with the average size of 342 nm as examined by DLS (Fig. S2†). As shown in Fig. 1b, the dispersion of MGO was slightly enhanced and the morphology of MGO was not obviously changed after modifying with MDP and FA compared with the undecorated MGO. The results of hysteresis regression curve showed that the saturation magnetization value of MGO-MDP–FA (30.18 emu g^{-1}) was slightly lower than

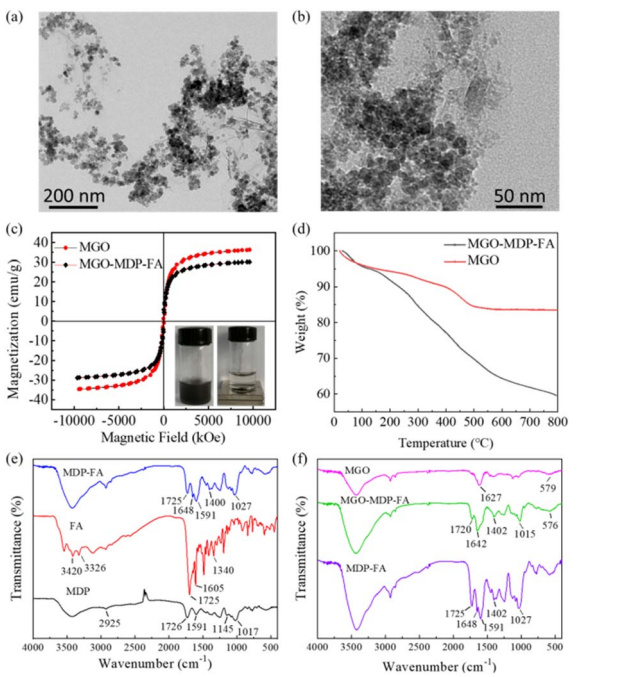

Fig. 1 TEM images of MGO (a) and MGO-MDP–FA (b); (c) magnetization curves of MGO and MGO-MDP–FA; (d) TGA curves of MGO and MGO-MDP–FA; (e) FTIR spectrum of FA, MDP and MDP–FA; (f) FTIR spectrum of MGO and MGO-MDP–FA.

that of MGO (36.26 emu g^{-1}), which might be due to the successful modification of MDP and FA (Fig. 1c). In addition, the XRD diffraction pattern of the MGO was showed in Fig. S3,† which in accordance with our previous work and six characteristic peaks at 2θ of MGO corresponding to the standard XRD data cards of Fe_3O_4 crystal (JCPDS no. 85-1436).[43,44]

FTIR spectra were measured to further verify the successful synthesis of MDP–FA and MGO-MDP–FA (Fig. 1e and f). For the spectra of MDP, the wide peak in the range of 3200–3600 cm^{-1} could be ascribed to the association peak of hydrogen bond and the peak at 2925 cm^{-1} could be confirmed as the stretching vibration of –C–H on the sugar ring skeleton. The vibration coupling peaks of –C–C at 1154 cm^{-1} and the anti-symmetric stretching vibration peak of C–O–C at 1017 cm^{-1} suggested that the existence of MD structure. In addition, the peak at 1725 cm^{-1} should be contributed to the stretching vibration of C=O of the carboxyl group of the PDA and the peak at 1591 cm^{-1} should be duo to the stretching vibration of C=C, which proved that the MD was successfully cross-linked with PDA. In the FITR spectra of MDP–FA, the stretching vibration of C=O bond of the carboxyl group at 1725 cm^{-1}, the stretching vibration of C=O of the amide bond at 1648 cm^{-1} and the stretching vibration of C–N at 1400 cm^{-1} indicated that FA was successfully grafted onto the MDP surface. In the FITR spectrum of MGO-MDP–FA, there was a new peak at 1642 cm^{-1}, which should be attributed to the stretching vibration of the C=O bond of the amide group. The peak at 1015 cm^{-1} could be ascribed to the stretching vibration of C–O–C of MDP. And the peak at 576 cm^{-1} was probably cause by the stretching vibration of Fe–O in MGO,[43,44] which indicated that MGO-MDP–FA was successfully prepared.

As shown in Fig. 1d, TGA was performed to further prove the successful preparation of the nanocomposite MGO-MDP–FA (heating rate was 10 °C min^{-1}). For the curve of MGO, the total weight loss was estimated to be 18% from 25 °C to 800 °C. The slight weight loss at low temperatures (<200 °C) might be attributed to the volatilization of residual water and solvent, the mass loss of 200–500 °C was likely to be attributed to the removal of the oxygen-containing functional groups of GO and the damage of –OH groups on the surface of Fe_3O4, and the left after 500 °C was likely to be Fe_3O_4 nanoparticles which are not easy to decompose.[45,46] According to the TGA diagram of MGO in air, the relative content of Fe_3O_4 nanoparticles in the composite was calculated to be 80% (Fig. S4†). However, for the MGO-MDP–FA, the total weight loss was estimated to be 40.48% from 25 °C to 800 °C. In the same condition, 29.18% of significant weight loss of MGO-MDP–FA in the range of 200–600 °C could be attributed to the decomposition of MDP and FA on the surface of MGO, and the further weight loss in the high temperature region (about 600–800 °C) was due to the skeleton damage of GO. Compared with the MGO, the much higher weight loss of MGO-MDP–FA was further demonstrated the successful grafting of MDP and FA on the MGO.

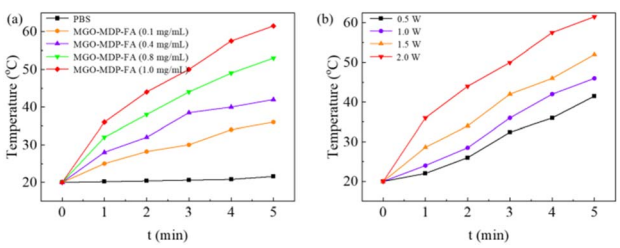

Fig. 2 (a) Temperature change curves of MGO-MDP–FA solution with different concentration under near-infrared laser irradiation (808 nm, 2.0 W cm^{-2}) for 5 min recorded by the thermal imager; (b) temperature rising curves of MGO-MDP–FA at the same concentration irradiated with different laser irradiation intensity (808 nm).

3.2 Photothermal performance of MGO-MDP–FA

To evaluate the photothermal performance of MGO-MDP–FA, we monitored the real-time temperature of MGO-MDP–FA in PBS irradiating with 808 nm NIR laser by the infrared thermal imaging system. As shown in Fig. 2a, the temperature changed from 21.6 °C to 61.5 °C as the concentration of MGO-MDP–FA changed from 0 mg mL^{-1} to 1.0 mg mL^{-1} with the irradiation of near-infrared laser (808 nm, 2.0 W cm^{-2}) for 5 min. In addition, the temperature of MGO-MDP–FA in PBS at the same concentration also rose with the increase of the laser power intensity (Fig. 2b). With the NIR laser irradiation intensity increased from 0.5 W cm^{-2} to 2.0 W cm^{-2}, the temperature of MGO-MDP–FA solution at the same concentration rose from 41.5 °C to 61.5 °C. The above results demonstrated that the photothermal conversion efficiency of MGO-MDP–FA was concerned with solution concentration and laser irradiation intensity.

Furthermore, we measured the photothermal effect of Fe_3O_4, GO and MGO respectively. As shown in the Fig. S5,† the photothermal effect of MGO is stronger than that of Fe_3O_4 and GO, and the photothermal effect of Fe_3O_4 is similar to GO. This result indicated that both Fe_3O_4 and GO have good photothermal conversion efficiency, and equally contribute to the photothermal effect of MGO.

3.3 Drug loading capacity of MGO-MDP–FA for DOX

As a multifunctional drug carrier, the drug loading capacity of MGO-MDP–FA was researched by fluorescence spectroscopy. As shown in Fig. S6,† in the concentration range of 5×10^{-4}–5×10^{-3} mg mL^{-1}, DOX had a good calibration curve ($R^2 = 0.9938$), which was used for subsequent calculation. Firstly, we researched the drug adsorption kinetic by measuring the loading quantity of DOX on MGO-MDP–FA with time-variation. As shown in Fig. 3a, the adsorption rate was the fastest as the initial DOX concentration was high in the first 200 min, the adsorption rate gradually slowed down as the concentration of DOX decreased within 200–400 min, and the adsorption was almost saturated and the adsorption rate was much at one after 400 min. Furthermore, Lagergren's pseudo-first-order kinetic model (eqn (S1)†) and Ho's pseudo-second-order kinetic model (eqn (S2)†) were used to study the probable drug adsorption mechanism. According to the linear fitting curves of Lagergren's pseudo-first-order kinetic model (Fig. 3b) and Ho's pseudo-second-order kinetic model (Fig. 3c), the kinetic parameters of two models were presented in Table S1.† It was obvious that the

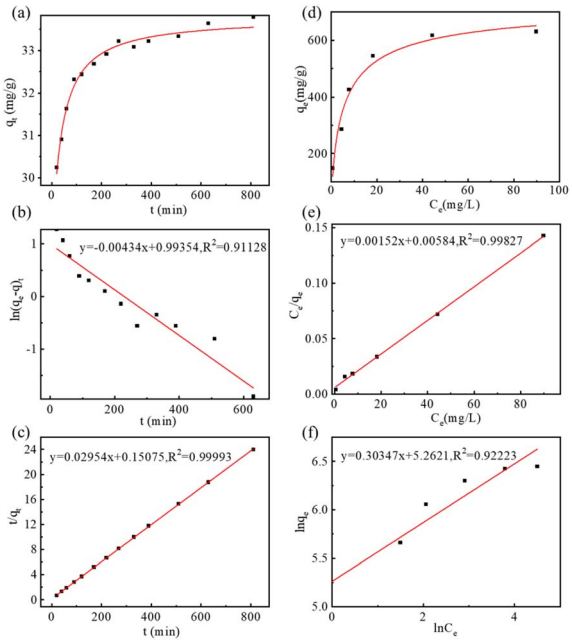

Fig. 3 (a) The drug adsorption kinetic curve of MGO-MDP–FA for DOX; linear fitting diagram with Lagergren's pseudo-first-order model (b) and Ho's pseudo-second-order model (c) for adsorption kinetics. (d) The adsorption isotherm curve of MGO-MDP–FA for DOX; linear fitting graphs of DOX on MGO-MDP–FA with Langmuir adsorption isotherm model (e) and Freundlich absorption isotherm model (f).

drug adsorption process of DOX onto MGO-MDP–FA was well corresponded with the Ho's pseudo-second-order kinetic model (R^2 = 0.99993), and the q_e value calculated following the Ho's pseudo-second-order kinetic model was nearer to the maximum drug loading in experiment, which indicated that chemical adsorption played a leading role in the interaction between DOX and MGO-MDP–FA probably focused on hydrogen bonding and π–π interaction.

In addition, the adsorption isotherm of MGO-MDP–FA for DOX was measured to determine the drug loading amount and explore the possible drug loading mechanism. As shown in Fig. 3d, the drug loading efficiency of DOX on MGO-MDP–FA gradually improved with the increase of DOX concentration. Moreover, the adsorption isotherm process was evaluated by the single-layer Langmuir isotherm adsorption model (eqn (S3)†) and the multi-layer Freundlich isotherm adsorption model (eqn (S4)†), the corresponding linear fitting curves of two models were displayed respectively in Fig. 3e and f, and the relevant parameters of two models was revealed in Table S2.† Compared with the Freundlich adsorption model, the isotherm adsorption process of DOX onto MGO-MDP–FA was more in line with the Langmuir adsorption model (R^2 = 0.99827), which indicated that the drug adsorption process was inclined to single-layer adsorption. In addition, the maximum drug loading amount of MGO-MDP–FA for DOX calculated *via* Langmuir adsorption model reached to 657.9 mg g^{-1} and the drug loading capacity (DLC) of MGO-MDP–FA was 39.68 wt%, which was considerably higher than that of the previously reported at the same concentration of DOX.[19,20]

3.4 Drug releasing performance of MGO-MDP–FA

The release behavior of DOX from MGO-MDP–FA in PBS with pH 5.3 and pH 7.4 at 37 °C was investigated by fluorescence spectroscopy. As shown in Fig. 4a, the release amount of DOX increased with the extension of time, but the drug releasing efficiency had no significant difference between PBS with pH 7.4 and PBS with pH 5.3. This phenomenon might be attributed to the tight connection between the drug and the nanocarrier, and the pH had no obvious effect on the interaction between them.

Furthermore, considering tumor tissue is an acidic environment and the excellent photothermal conversion effect of MGO, we investigated the NIR-stimulative drug releasing of DOX from MGO-MDP–FA at pH 5.3 under the NIR laser irradiation for 5 min. As revealed in Fig. 4b, the drug release amount reached up to 50.24% under the irradiation of NIR, which was 1.84-fold than that without NIR irradiation at pH 5.3. Therefore, the NIR-stimulative drug releasing performance indicated that local high temperature induced by photothermal effect could promote the release of drugs at the tumor site and enhanced effect of chemotherapy, which provided the possibility for the chemo-photothermal co-treatment of tumors.

3.5 Biocompatibility and stability

Good blood compatibility is the precondition to ensure the nanometer drug carrier enter the organism smoothly and functioning normally.[47] The hemolysis analysis of MGO-MDP–FA was performed to evaluate the blood compatibility *in vitro*. The percentage of hemolysis and the corresponding image of hemolysis were showed in Fig. 5a. Compared with the negative control group, there were no obvious hemolysis phenomenon within a certain concentration range (0.1–0.4 mg mL^{-1}), and the percentage of hemolysis was less than one percent as the concentration of MGO-MDP–FA up to 0.4 mg mL^{-1}. This demonstrated that our synthesized nano-drug carrier MGO-MDP–FA had excellent blood compatibility, which provided a powerful piece of evidence for the safe existence of MGO-MDP–FA nano-drug vector *in vitro*.

In addition, we evaluated the stability of the MGO-MDP–FA *in vitro* through comparing the UV-vis absorption spectrum of the newly prepared MGO-MDP–FA aqueous solution and the MGO-MDP–FA aqueous solution placed for one month. As shown in Fig. 5b, there was no significant difference between the UV-vis spectra of newly prepared and placed for one month,

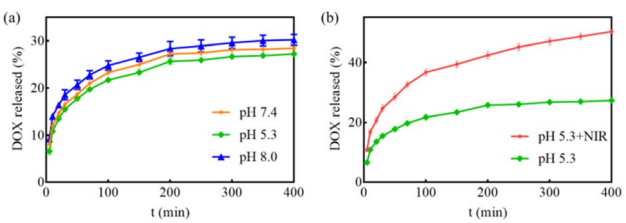

Fig. 4 (a) The drug releasing rate of DOX from MGO-MDP–FA in PBS with pH 7.4 and 5.3 at 37 °C; (b) the release amount of DOX from MGO-MDP–FA in PBS at pH 5.3 with or without NIR laser irradiation (808 nm, 2.0 W cm^{-2}).

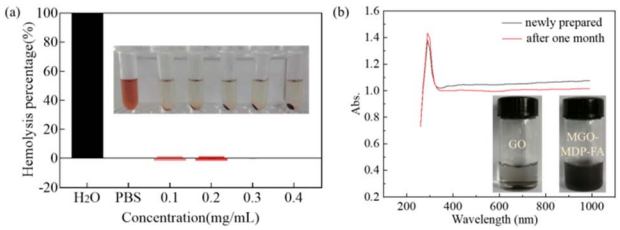

Fig. 5 (a) The percentage of hemolysis and the corresponding hemolysis phenomenon of MGO-MDP–FA with concentrations of 0.1, 0.2, 0.3 and 0.4 mg mL^{-1}, and the deionized water as the positive control (+), PBS solution as the negative control (−). Data are shown as mean ±SD ($n = 3$); (b) UV-vis spectra of newly prepared MGO-MDP–FA aqueous solution and the MGO-MDP–FA aqueous solution placed for one month.

indicating that MGO-MDP–FA had well stability *in vitro* over a long period of time. Furthermore, there was no significant change in UV absorption of MGO-MDP–FA@DOX solution after one month at room temperature, indicating that DOX had no obvious leakage and MGO-MDP–FA@DOX had good stability (Fig. S7†).

3.6 Anti-tumor activity of MGO-MDP–FA *in vitro*

3.6.1 Cellular uptake. In order to verify the cancer cell targeting ability of MGO-MDP–FA@DOX *in vitro*, we investigated the cellular uptake of MGO-MDP–FA@DOX by human-derived liver cancer cells (HepG2), human breast cancer cell (HeLa) and human normal cervical epithelial cells (HUCEC). As shown in Fig. 6a–c, the red fluorescence of MGO-MDP–FA@DOX gradually increased over time in three kinds of cells, especially in HepG2 and HeLa cells. More importantly, compared with HUCEC cells, there was the stronger red fluorescence in HepG2 cells and HeLa cells (Fig. 6a). This phenomenon could be attributed to the FA of MGO-MDP–FA@DOX specifically bound with the folate receptor over-expressing on the cancer cell surface.

To further verify the targeting ability of MGO-MDP–FA@DOX for cancer cell, three kinds of cells were co-cultured with MGO-MDP–FA@DOX + FA for 5 h. As shown in Fig. 6d and e, compared with co-cultured with the MGO-MDP–FA@DOX for 5 h, HepG2 cells and HeLa cells treated with MGO-MDP–FA@DOX + FA showed relatively weak red fluorescence and only few of the cells had red fluorescence. However, there were no distinct difference of red fluorescence between MGO-MDP–FA@DOX and MGO-MDP–FA@DOX + FA in HUCEC cells (Fig. 6f). It demonstrated that the addition of FA inhibited the uptake of MGO-MDP–FA@DOX by HepG2 cells and HeLa cells, which indicated that modification with FA could significantly enhance the cancer cell targeting ability of the MGO-MDP–FA@DOX. In addition, the intracellular red fluorescence intensity of the MGO-MDP–FA with modification of FA was stronger than that of the MGO-MDP without modification of FA in HepG2 and HeLa cells, indicating that the amount of MGO-MDP–FA entering tumor cells was more than that of MGO-MDP, further demonstrating the active tumor targeting effect of FA (Fig. 7a and b).

The purpose of nano-drug delivery system is to deliver the moderate amounts of drugs to the right place at the proper time, so as to improve the efficiency of drug utilization and reduce the toxic side effects on normal tissues. Therefore, we evaluated the tumor targeting ability of MGO-MDP and MGO-MDP–FA *in vivo*. As shown in Fig. 7c, it could be observed that the temperature at the tumor site of mice in the MGO-MDP–FA group (46.9 °C) was significantly higher than that in the PBS group (38.3 °C) and the MGO-MDP group (40.8 °C). This result indicated that MGO-MDP can be passively targeted to the tumor site through EPR effect, and the MGO-MDP–FA group could further concentrate in the tumor site as the modification of FA with active targeting the tumor, which was consistent with the results of *in vitro* experiments, and further demonstrated the tumor targeting effect of MGO-MDP–FA *in vivo*.

3.6.2 Cytotoxicity test. Counting Kit-8 (CCK-8) test was used to evaluate the anti-tumor activity of MGO-MDP–FA@DOX *in vitro*. Firstly, we could clearly see that there was no obvious toxic effect on normal cell (HUCEC) in each group except DOX group in Fig. 8a, which indicated that the MGO-MDP–FA or MGO-MDP–FA@DOX had good biocompatibility *in vitro*. In addition,

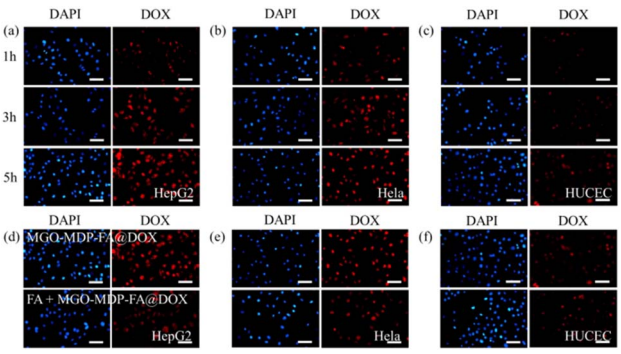

Fig. 6 The cellular uptake of MGO-MDP–FA@DOX by HepG2 (a), HeLa (b), HUCEC (c) cells at 1 h, 3 h and 5 h observed under the fluorescent inverted microscope, the red fluorescence was the natural fluorescence of DOX. Fluorescence microscope image of HepG2 (d), HeLa (e), HUCEC (f) cells incubated with or without FA for 1 h and with MGO-MDP–FA@DOX for 5 h (scale bar = 50 μm).

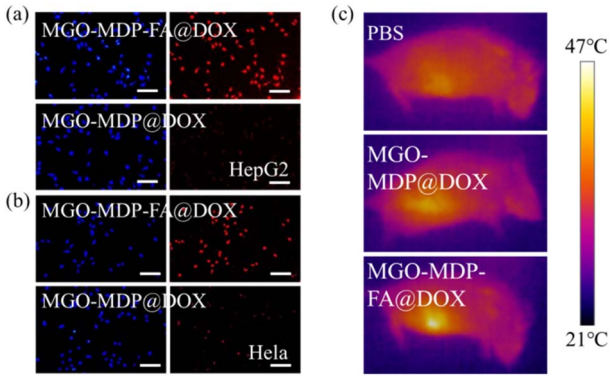

Fig. 7 Fluorescence microscope image of HepG2 (a) and HeLa (b) cells incubated with MGO-MDP–FA@DOX or MGO-MDP@DOX for 5 h. (c) Thermal imaging of tumor sites treated with PBS, MGO-MDP@DOX and MGO-MDP–FA@DOX under NIR irradiation (808 nm, 2 W cm^{-2}) for 5 min.

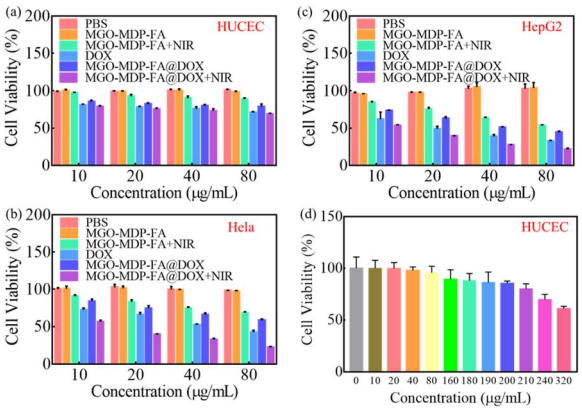

Fig. 8 Cell viability of HUCEC (a); HepG2 (b); HeLa (c) treated with PBS, MGO-MDP–FA, MGO-MDP–FA + NIR, DOX, MGO-MDP–FA@DOX and MGO-MDP–FA@DOX + NIR. (among them, the concentrations of MGO-MDP–FA and MGO-MDP–FA@DOX were 10, 20, 40 and 80 μg mL^{-1}, respectively). (d) Cell viability of HUCEC treated with MGO-MDP–FA in different concentration.

the cell viability of HepG2 and HeLa cells treated with MGO-MDP–FA was close to 95%, the cell viability continued to be close to 90% as the concentration of MGO-MDP–FA up to 80 μg mL^{-1} (Fig. 8c and d) and the cell survival rate was as high as 80% even when the concentration of MGO-MDP–FA was 210 μg mL^{-1}, indicating that the dark toxicity of MGO-MDP–FA was negligible (Fig. 8b). And it could be obviously seen from Fig. 8c and d that the cell killing efficiency possessed concentration-dependent of each group in HepG2 and HeLa cells. Moreover,

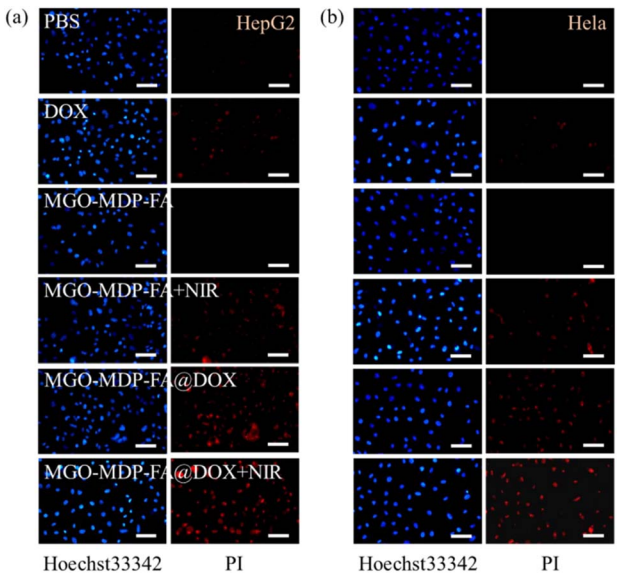

Fig. 9 Fluorescence microscopy images of HepG2 (a), HeLa (b) cells were incubated with PBS, MGO-MDP–FA, DOX, MGO-MDP–FA@DOX, MGO-MDP–FA + NIR, MGO-MDP–FA@DOX + NIR, and stained with the Apoptosis and Necrosis Assay Kit (double staining method with Hoechst 33342 and PI). The normal cells showed weak blue and weak red fluorescence, the apoptotic cells showed strong blue and weak red fluorescence and the necrotic cells showed strong blue and strong red fluorescence (scale bar = 100 μm).

the cell viability of HepG2 cells and HeLa cells were similar. For example, in HepG2 cells, the cell viability of MGO-MDP–FA@DOX group was about 44.2% as the concentration up to 80 μg mL^{-1}. And the cell viability of MGO-MDP–FA + NIR group was about 53.3%, which revealed MGO-MDP–FA possessed excellent photothermal conversion efficiency. More important, in MGO-MDP–FA@DOX + NIR group, the cell viability of 21.2% was lower than the DOX group (32.5%), which indicated that the combined effect of chemotherapy and photothermal therapy was better than that of single chemotherapy.

3.6.3 Apoptosis staining. We used the Apoptosis and Necrosis Assay Kit (double staining method with Hoechst 33342 and PI) to further demonstrate the anti-tumor effect of MGO-MDP–FA@DOX on HepG2 and HeLa cells *in vitro*. As shown in Fig. 9, the MGO-MDP–FA group exhibited weak blue fluorescence and weak red fluorescence, indicating that MGO-MDP-FA showed good biocompatibility *in vitro*. In addition, for MGO-MDP–FA@DOX group and MGO-MDP–FA + NIR group, there were bright blue fluorescence and weak red fluorescence emerged into most of the cells and bright blue and bright red fluorescence emerged into a small number of cells. It was demonstrated that MGO-MDP–FA not only can realize chemotherapy as a multifunctional drug carrier, but also can realize photothermal therapy as an excellent photothermal material. What's more, compared with DOX group, almost all of cells in MGO-MDP–FA@DOX + NIR group exhibited bright blue fluorescence and bright red fluorescence, which was consistent with the result of CCK-8.

4. Conclusion

To sum up, a novel nano-drug delivery system MGO-MDP–FA was successfully constructed in this paper for dual-targeted chemo-photothermal therapy of cancer. The nano-drug carrier combined the targeting effect of FA on cancer cells and the magnetic targeting effect of MGO, which ensured that the nano-drug carrier can accurately target cancer cells and reduce the toxic side effects on the surrounding normal tissues. In addition, the large specific surface area of MGO nanomaterials and the modification of MDP polymer enabled the nano-drug carrier to effectively load a large number of anticancer drugs, and it also has the NIR-stimulating release performance. Based on the excellent photothermal conversion efficiency of MGO nanomaterials, MGO-MDP–FA could be used in the synergistic treatment of cancer chemotherapy and photothermal therapy *in vitro*. In brief, the novel nano-drug delivery system had potential applications in the integration of cancer diagnosis and treatment.

Conflicts of interest

There are no conflicts to declare.

Acknowledgements

This work was financially supported by the National Natural Science Foundation of China (No. 21976113), the Basic

Research Project of Shanxi Province (No. 202103021224240, 202103021224238, 20210302123322), and Research Project Supported by Shanxi Scholarship Council of China (No. 2021-081).

References

1 H. S. Han and K. Y. Choi, *Biomedicines*, 2021, **9**, 305.
2 J. Q. Chen, C. Y. Ning, Z. N. Zhou, *et al*, *Prog. Mater. Sci.*, 2019, **99**, 1–26.
3 V. D. Nguyen, H. K. Min, D. H. Kim, *et al*, *ACS Appl. Mater. Interfaces*, 2020, **12**, 10130–10141.
4 X. Y. Deng, H. Liang, W. B. Yang, *et al*, *J. Photochem. Photobiol., B*, 2020, **208**, 111913.
5 Q. Li, L. Hong, H. H. Li, *et al*, *Biosens. Bioelectron.*, 2017, **89**, 477–482.
6 K. J. Lagos, H. H. Buzzá, V. S. Bagnato, *et al.*, *Int. J. Mol. Sci.*, 2021, **23**, 22.
7 X. J. Liu, I. Marangon, G. Melinte, *et al.*, *ACS Nano*, 2014, **8**, 11290–11304.
8 R. Singh and S. V. Torti, *Adv. Drug Delivery Rev.*, 2013, **65**, 2045–2060.
9 A. Granja, M. Pinheiro, C. T. Sousa, *et al.*, *Biochem. Pharmacol.*, 2021, **190**, 114639.
10 H. S. Kim and D. Y. Lee, *Polymers*, 2018, **10**, 961.
11 R. S. Riley and E. S. Day, *Wiley Interdiscip. Rev.: Nanomed. Nanobiotechnol.*, 2017, **9**, 1449.
12 Y. L Dai, H. T. Bi, X. R. Deng, *et al*, *J. Mater. Chem. B*, 2017, **5**, 2086–2095.
13 Z. X. Zhao, Y. Z. Huang, S. G. Shi, *et al*, *Nanotechnology*, 2014, **25**, 285701.
14 R. Riedel, N. Mahr, C. Y. Yao, *et al*, *Nanoscale*, 2020, **12**, 3007–3018.
15 D. D. Chai, B. J. Hao, R. Hu, *et al*, *ACS Appl. Mater. Interfaces*, 2019, **11**, 22915–22924.
16 J. Beik, Z. Alamzadeh, M. Mirrahimi, *et al*, *ACS Appl. Bio Mater.*, 2021, **4**, 4280–4291.
17 L. Yang, T. H. Kim, H. Y. Cho, *et al*, *Adv. Funct. Mater.*, 2021, **31**, 2006918.
18 K. Kostarelos, A. Bianco and M. Prato, *Nat. Nanotechnol.*, 2009, **4**, 627–633.
19 S. Y. Madani, N. Naderi, O. Dissanayake, *et al.*, *Int. J. Nanomed.*, 2011, **6**, 2963–2979.
20 C. Wells, O. Vollin-Bringe, V. Fiegel, *et al.*, *Adv. Funct. Mater.*, 2018, **28**, 1706996.
21 S. J. Cheng, H. Y. Chiu, P. V. Kumar, *et al*, *Biomater. Sci.*, 2018, **6**, 813–819.
22 K. Vinothini, N. K. Rajendran, A. Ramu, *et al*, *Biomed. Pharmacother.*, 2019, **110**, 906–917.
23 R. K. Thapa, J. Y. Choi, B. K. Poudel, *et al*, *Int. J. Nanomed.*, 2016, **11**, 2799–2813.
24 H. Chen and E. Ruckenstein, *J. Phys. Chem. Lett.*, 2014, **5**, 2979–2982.
25 K. Wang, J. Ruan, H. Song, *et al*, *Nanoscale Res. Lett.*, 2010, **6**, 8.
26 N. Karki, H. Tiwari, M. Pal, *et al*, *Colloids Surf., B*, 2018, **169**, 265–272.
27 T. Figueroa, C. Aguayo and K. Fernández, *Int. J. Nanomed.*, 2020, **15**, 1229–1238.
28 P. M. Sivakumar, M. Islami, A. Zarrabi, *et al*, *Anti-Cancer Agents Med. Chem.*, 2020, **20**, 1340–1351.
29 R. Ferrari, G. Storti and M. Morbidelli, *J. Polym. Sci.*, 2020, **58**, 1642–1654.
30 A. Das, S. Ray, U. Raychaudhuri, *et al*, *Int. Food Res. J.*, 2017, **24**, 720–725.
31 N. Wathoni, S. Uray and C. Insani, *J. Appl. Pharm. Sci.*, 2013, **3**, 68–71.
32 S. Yan, J. Ren, Y. Jian, *et al*, *Biomacromolecules*, 2018, **19**, 4554–4564.
33 A. B. Shreya, S. Y. Raut and R. S. Managuli, *AAPS PharmSciTech*, 2018, **20**, 15.
34 M. M. Agwa and S. Sabra, *Int. J. Biol. Macromol.*, 2021, **167**, 1527–1543.
35 B. Liu, W. Yang, C. Che, *et al*, *ChemistryOpen*, 2021, **10**, 408–413.
36 X. Geng, D. Gao, D. Hu, *et al*, *ACS Appl. Mater. Interfaces*, 2020, **12**, 55624–55637.
37 Y. Xu, H. Wu, J. Huang, *et al.*, *Theranostics*, 2020, **10**, 2479–2494.
38 P. Sun, N. Zhang, Y. Tang, *et al*, *Int. J. Nanomed.*, 2017, **12**, 2657–2672.
39 S. B. Ghaffari, M. H. Sarrafzadeh, Z. Fakhroueian, *et al*, *Mater. Sci. Eng., C*, 2019, **103**, 109827.
40 W. Liang, C. Yang, D. Zhou, *et al*, *Chem. Commun.*, 2013, **49**, 3510–3512.
41 W. Liang, Y. Huang, D. Lu, *et al*, *Polymers*, 2019, **11**, 133.
42 C. Wen, R. Cheng, T. Gong, *et al*, *Colloids Surf., B*, 2020, **199**, 111510.
43 X. Wang, Q. Ma, C. Wen, *et al*, *RSC Adv.*, 2021, **11**, 39804–39812.
44 T. Gong, X. Wang, Q. Ma, *et al*, *J. Inorg. Biochem.*, 2021, **223**, 111558.
45 Y. H. Zhou, L. L. Sun, H. X. Wang, *et al*, *Mater. Chem. Phys.*, 2016, **170**, 83–89.
46 T. Gong, Y. H. Zhou, L. L. Sun, *et al*, *RSC Adv.*, 2016, **6**, 80955–80963.
47 H. Zhang, Y. Li, Z. Pan, *et al*, *Mol. Pharm.*, 2019, **16**, 1982–1998.